JOURNAL OF MATERIALS SCIENCE **32** (1997) 2883–2894

Microstructure, tensile deformation and fracture behaviour of aluminium alloy 7055

T. S. SRIVATSAN, S. SRIRAM
Department of Mechanical Engineering, The University of Akron, Akron, OH 44325, USA
D. VEERARAGHAVAN, V. K. VASUDEVAN
Department of Materials Science and Engineering, University of Cincinnati, Cincinnati, OH 45221, USA

The microstructure, tensile deformation and fracture behaviour of aluminium alloy 7055 were studied. Detailed optical and electron microscopy observations were made to analyse the as-received microstructure of the alloy. Detailed transmission electron microscopy observations revealed the principal strengthening precipitates to be the hexagonal disc-shaped η' phase of size 2 mm × 20 mm and fully coherent with the aluminium alloy matrix, the presence of spheroidal dispersoids, equilibrium grain-boundary η precipitates and narrow precipitate-free zones adjacent to grain-boundary regions. It is shown that microstructural characteristics have a profound influence on tensile deformation and fracture behaviour. Tensile test results reveal the alloy to have uniform strength and ductility in the longitudinal and transverse orientations. Strength marginally decreased with an increase in test temperature but with a concomitant improvement in elongation and reduction in area. No change in macroscopic fracture mode was observed with sample orientation. Fracture, on a microscopic scale, was predominantly ductile comprising microvoid nucleation, growth and coalescence. The tensile deformation and fracture process are discussed in the light of the competing influences of intrinsic microstructural effects, matrix deformation characteristics, test temperature and grain-boundary failure.

1. Introduction

The development of aerospace materials is driven by a fascinating mix of scientific, economical and also military motivations. In today's environment the aerospace industry is showing a shift from a defense-driven condition that pushed technology to its limits, to one largely dictated by commercial interests. This led to an increased emphasis on issues like off-the-shelf availability, cost effectiveness, damage tolerance, durability, and high life-cycle designs, as primary considerations in materials development and selection. This provided the necessary impetus to material scientists and engineers to make material refinements while concurrently engineering new alloys and innovative processing (both primary and secondary) techniques, for a multitude of products, effectively to meet the increased demands set by the newer generation of aircraft. Among the candidate materials available to meet the challenges of modern airframe design, is aluminium. In fact, the sustained success achieved with aluminium alloys and assisted by the tried-and-true design concept coupled with a record of continuous improvements and cost-effectiveness, has provided much reluctance to the selection and use of alternative materials. However, extensive use of the age-hardenable 2XXX-series and 7XXX-series alloys at high strength levels, was hampered by poor secondary properties of toughness, stress corrosion cracking (SCC), and cyclic fatigue resistance, particularly in the short transverse direction. The importance of these materials in airframe construction, coupled with an increased emphasis on reducing weight and increasing the speed of aircraft, has stimulated considerable scientific interest in using microstructural control as an attractive and viable means to improve these properties [1]. Microstructural control can be systematically achieved through (a) changes in alloy chemistry [2–4], (b) use of different grain-refining elements [4], (c) minimizing the level of impurity elements such as iron and silicon [5, 6], and (d) novel thermomechanical processing treatments [7–13]. This culminated in a spectrum of derivative alloys and tempers.

The development of T7X-type temper for the Al–Zn–Mg–Cu alloy 7075 solved problems associated with SCC and exfoliation corrosion [13, 14]. However, the weight of the component increased, primarily because of the lower strength of the 7075 products in these tempers [13, 14]. This resulted in compositional modifications and thus the development and emergence of aluminium alloy 7050 in the T6, T76 and T74 tempers. The attractive combination of strength, corrosion characteristics and SCC resistance of alloy 7050 was attributed to increased copper content relative to that of alloy 7075. The higher copper content

0022–2461 © *1997 Chapman & Hall*

provides a modification in the relative differences in electro-chemical potential between the matrix and grain-boundary regions [13]. The continuing need for increased strength, while concurrently retaining the durability and damage tolerance characteristics of alloy 7050, led to the development and emergence of alloy 7150–T77. However, for compression-dominated airframe applications, such as the upper wing structure of large commercial aircraft, the requirement of a moderate level of fracture toughness, cost-effective weight reduction, improved corrosion resistance, durability, and damage tolerance, led to modifications in the composition limits and heat treatment of alloy 7150 and resulted in the emergence of alloy 7055. An attempt to improve the resistance of alloy 7055 to exfoliation corrosion, without sacrificing strength, resulted in the development of a proprietory temper designated by the Aluminum Company of America (ALCOA) as T77. Alloy 7055-T77 plate offers a strength increase of about 10% relative to that of 7150-T6, and 30% higher than that of 7075-T76. It also offers high fracture toughness and resistance to the growth of fatigue cracks [13, 14]. The attractive combination of properties of 7055-T77 was attributed to its high ratios of Zn/Mg and Cu/Mg [13]. When processed to the T77 temper, the 7055 composition provides a microstructure at and near grain boundaries that is resistant to both intergranular fracture and intergranular corrosion. The matrix microstructure resists strain localization, while maintaining a high resistance to the passage of dislocations [13].

The objective of this work was to record the microstructure, tensile deformation and fracture characteristics of alloy 7055-T7751. The quasi-static fracture behaviour of the alloy was examined in the light of the mutually interactive influences of intrinsic microstructural features, matrix deformation characteristics, and micromechanisms which promote failure.

2. Experimental procedure

2.1. Material

The 7055 aluminium alloy used in this experimental investigation was provided by the Aluminum Company of America (ALCOA) as 25 mm thick extruded plate in the T7751 condition. The nominal chemical composition (wt %) of the alloy is shown in Table I. This alloy is a modified version of alloy 7150 with lower levels of the impurity elements. Zirconium present in the alloy controls the grain size and suppresses recrystallization. It combines with aluminium to form the metastable Al_3Zr phase (β') that precipitates during ingot pre-heat and homogenization treatment. These particles, referred to as dispersoids, play an important role in controlling the deformation and fracture process. The T7751 temper designation refers to a proprietory thermomechanical treatment which involves solution heat treatment, water quench and a permanent stretch prior to artificial ageing. The higher solute (copper) content, compared with alloy 7150, provides the alloy with superior combinations of strength and ductility [14].

TABLE I Nominal chemical composition (wt %) of aluminium alloy 7055-T7751 (1.048 in. thick rolled plate)

Cu	Mg	Zn	Zr	Mn	Cr	Al
2.41	2.00	8.20	0.11	0.005	0.003	Balance

2.2. Techniques

Cylindrical test specimens, conforming to specifications in ASTM: E8-93 [15], were precision machined from the as-received 7055-T7751 plate. The stress axis of the specimens were parallel (longitudinal) and perpendicular (transverse) to the rolling direction. The test specimens measured 25 mm in length and 6.25 mm in diameter. To minimize the effects of surface irregularities, final surface preparation was achieved by mechanically polishing the gauge sections using 600-grit emery paper and then fine polishing to remove any and all circumferential scratches and surface machining marks.

Uniaxial tensile tests were performed up to failure on a fully automated, closed-loop, servohydraulic mechanical test machine (Instron) equipped with a 100 kN load cell. The specimens were deformed at a constant strain rate of $10^{-4}\,s^{-1}$. The tests were performed in controlled laboratory air environment (relative humidity of 55%) at ambient 27 °C and elevated 100 °C temperatures. The elevated temperature tests were conducted using an Instron Environmental Chamber (Model 3111). The temperature was controlled with the aid of a temperature controller fixed on the specimen's surface. Maximum temperature variation was well within 2 °C of the set-point temperature over the test duration. Ambient temperature varied from 27–29 °C with a maximum 2 °C variation during any given test. Before each test, the specimen was maintained or soaked at the test temperature for 30 min so as to achieve stability with the environment. The axial strain was measured using a dynamic 12.7 mm clip-on extensometer fixed, using rubber bands for room-temperature tests and steel springs for the elevated temperature tests, to the specimen gauge section. The stress and strain measurements, parallel to the load line, were recorded on a PC-based data acquisition system.

Metallographic samples were cut from the three orthogonal directions of the as-received plate. The samples were mounted in bakelite and wet ground on 320, 400 and 600 grit silicon carbide paper using water as lubricant. Subsequently, the ground samples were mechanically polished using 1 μm alumina-based polishing compound. The polished samples were etched with Keller's reagent and examined in an optical microscope and photographed using a standard bright-filled illumination technique to reveal the grain boundaries and overall grain morphology. Fine microstructural features were revealed by transmission electron microscopy (TEM). Thin foils for TEM investigation were prepared from 3 mm diameter discs punched out from 0.5 mm thick slices, cut at 90° to the stress axis from both the grip and gauge sections (just beneath the fracture surface), ground and thinned by electropolishing using a solution mixture of 30% nitric acid in methanol as the electrolyte, maintained at a temperature of $-20\,^{\circ}$C and at a potential difference of 15 V. The foils were examined in a Philips CM 20 transmission electron microscope (TEM) operating at 200 kV, and photographs under bright-field (BF), dark-field (DF) and selected-area diffraction (SAD) modes recorded. To aid in the interpretation of the experimental electron diffraction patterns, computer simulations were performed utilizing the Virtual Laboratories Desktop Microscopist® software.

Fracture surfaces of the deformed tensile samples were examined in a scanning electron microscope (SEM) to (a) determine the macroscopic fracture mode, and (b) characterize the fine-scale topography and microscopic mechanisms governing quasi-static fracture. The distinction between the macroscopic mode and microscopic fracture mechanism is based on the magnification level at which the observations are made. The macroscopic mode refers to the nature of failure (plane strain, plane stress or a combination of both), while the microscopic mechanism relates to the local failure process (microvoid formation, growth, coalescence and nature of microcracking). Samples for SEM observation were obtained from the deformed tensile specimens by sectioning parallel to the fracture surface.

3. Results and discussion

3.1. As-received microstructure

The microstructure of the as-received 7055 alloy is shown in Figs 1 and 2 as triplanar optical micrographs illustrating the grain structure and constituent particle distribution in the three orthogonal directions of the wrought plate. The microstructure was partially recrystallized with fairly large recrystallized grains that were flattened and elongated parallel to the longitudinal (rolling) direction, as a direct consequence of the deformation introduced by the rolling operation. The unrecrystallized regions comprise of both subgrains (with low-angle grain boundaries) and very fine recrystallized grains (with high-angle grain boundaries). On account of the very fine nature of this mixed structure and the intrinsic difficulty in distinguishing between these two components, entire regions of this nature are designated as being "unrecrystallized". The recrystallized grain size was non-uniform along each of the three orthogonal directions of the wrought plate, resulting in an anisotropic microstructure. At higher magnifications, the insoluble iron-rich intermetallic particles and partially soluble constituent particles were observed to be isolated and randomly distributed in the three orthogonal directions of the as-received plate. The final size of these intermetallic particles depends upon the fabrication procedure and ranges in size from 1–12 μm [16].

Transmission electron microscopy observations of the thin foils prepared from the undeformed grip section of the tensile sample revealed the following points:

(a) very well-defined grains of non-uniform size in the recrystallized regions (Fig. 3);

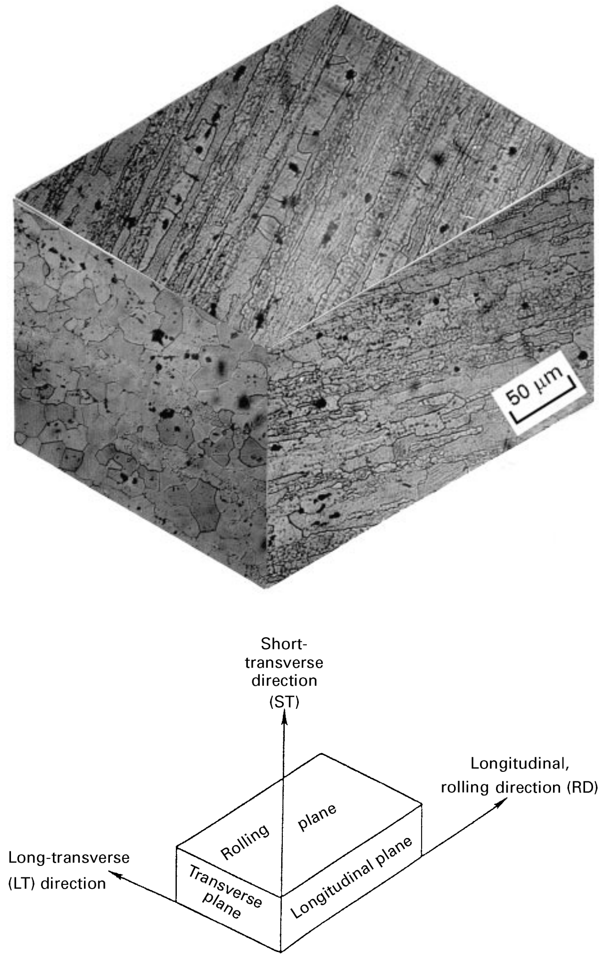

Figure 1 Triplanar optical micrograph illustrating the grain morphology of aluminium alloy 7055.

(b) a very fine dispersion of hexagonal disc-shaped precipitates of the intermediate η' phase with average dimensions of 2 nm × 20 nm (thickness × diameter) in the alloy matrix (see bright-field/dark-field images in Fig. 4a and b and corresponding SAD patterns in Fig. 5);

(c) a random distribution of spheroidal β' (Al_3Zr) precipitates with average diameter of 24 nm (see dark-field image in Fig. 4c and corresponding SAD patterns in Fig. 5);

(d) disc-shaped precipitates of the equilibrium η phase with average dimensions of 15 nm × 55 nm decorating grain boundaries, together with narrow precipitate-free zones (PFZs) around them (Fig. 6).

The intermediate η' precipitate is the most important strengthening phase in age-hardenable Al–Zn–Mg alloys, whereas the β' (Al_3Zr) dispersoids (f.c.c.-based $L1_2$, Cu_3Au structure) is a metastable phase that appears due to the presence of zirconium in the 7055 aluminium alloy. The presence of both of these phases was established by analysing SAD patterns recorded along a number of zone axes. In Fig. 5, pairs of experimental and computer-simulated SAD patterns corresponding to the $[0\bar{1}1]$Al (Fig. 5a, d), $[1\,1\,1]$Al (Fig. 5b, e) and $[1\,0\,0]$Al (Fig. 5c, f) zone axes are shown. The η' reflections in these patterns could be accounted for on the basis of a hexagonal structure with lattice parameters $a = 0.5078$ nm and $c = 1.395$

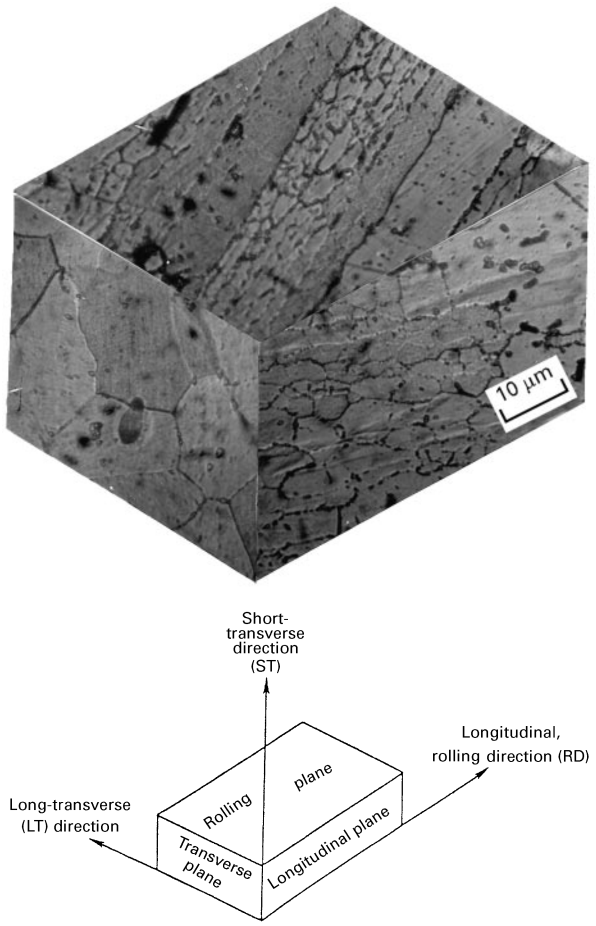

Figure 2 Triplanar optical micrograph illustrating constituent particle density and distribution along the three orthogonal directions of the wrought plate.

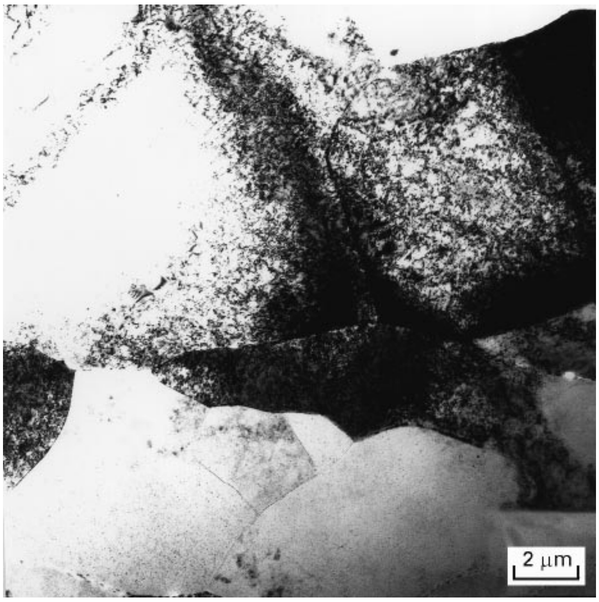

Figure 3 Low-magnification bright-field transmission electron micrograph showing well-defined grains of non-uniform size in the recrystallized region in the as-received 7055 aluminium alloy.

nm and an orientation relationship with the aluminium matrix given by

$$(1\,1\,1)\mathrm{Al} \parallel (0\,0\,0\,1)\eta'$$

$$[0\,\bar{1}\,1]\mathrm{Al} \parallel [1\,0\,\bar{1}\,0]\eta'$$

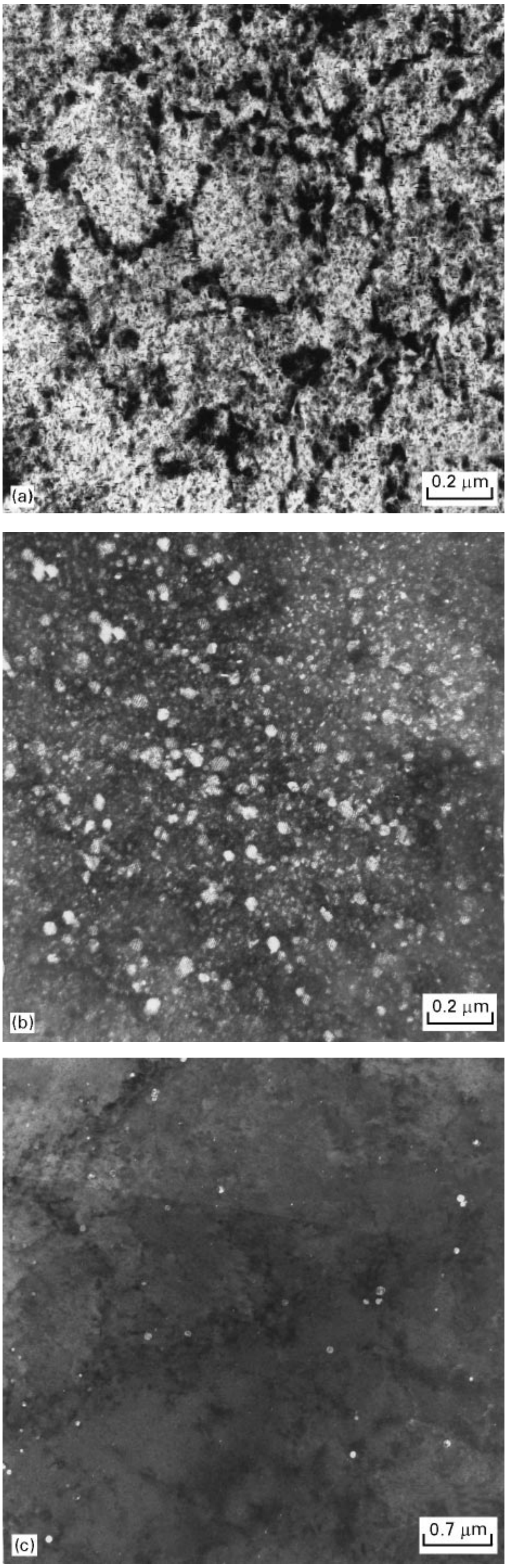

Figure 4 Transmission electron micrographs showing η′ and β′ (Al_3Zr) precipitates in the aluminium matrix. (a) Bright-field micrograph (η near $[0\,\bar{1}\,1]$); (b) dark-field micrograph taken using the $(\bar{2}\,1\,1\,0)$ η′ reflection (η near $[1\,1\,1]$); (c) dark-field micrograph taken using the $(0\,0\,1)$ β′-Al_3Zr superlattice reflection (η near $[1\,0\,0]$).

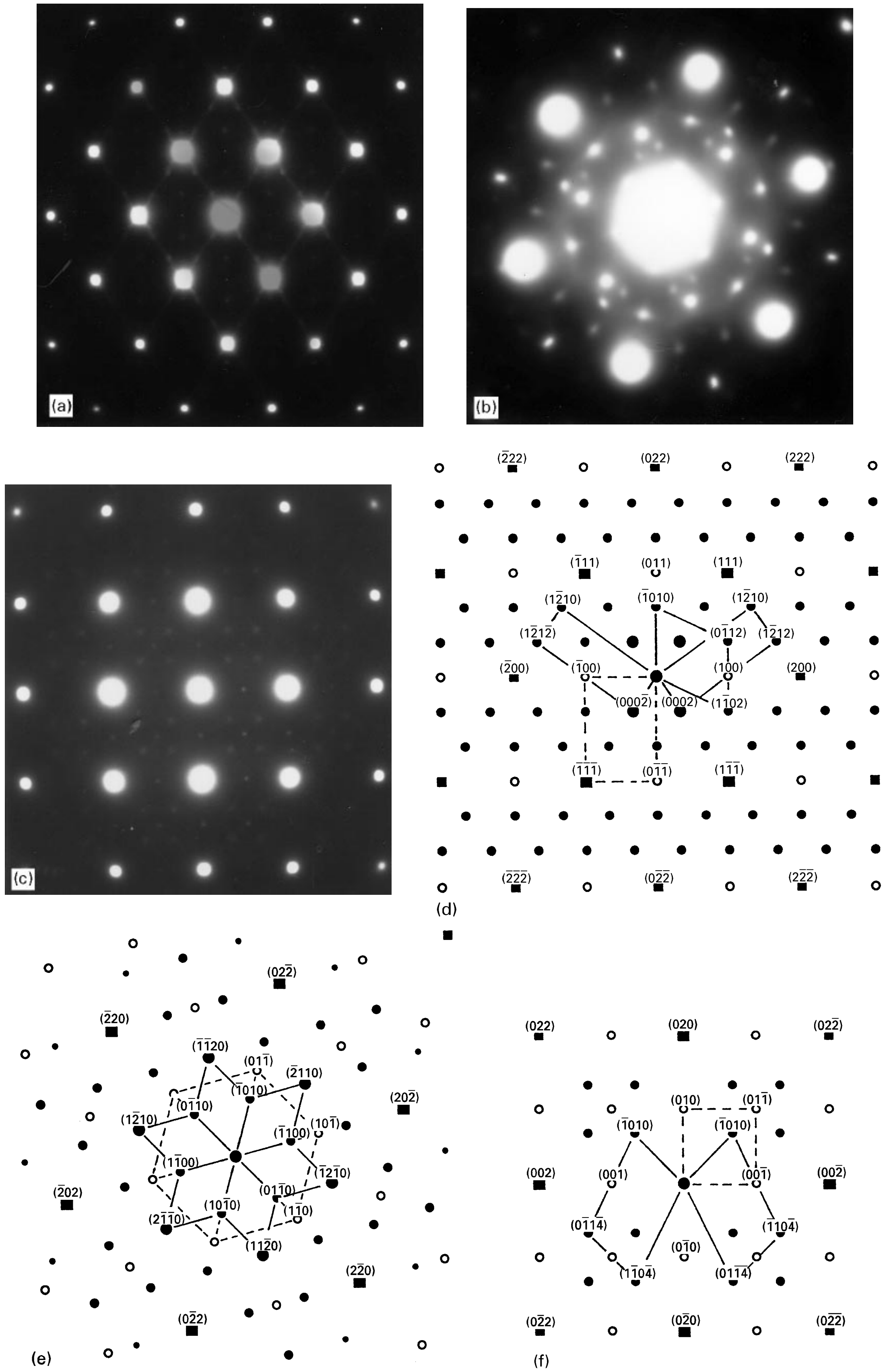

Figure 5 Pairs of experimental and computer-simulated [0 $\bar{1}$ 1] Al (a, d), [1 1 1] Al (b, e) and [1 0 0] Al (c, f) SAD patterns showing reflections from the aluminium matrix, η' and Al_3Zr precipitates. In (d, e, f), reflections from (■) aluminium matrix, (●) η' and (○) β'-Al_3Zr; outline of reflections from an η' variant, (----) outline of β'-Al_3Zr superlattice reflections.

Previously, Park and Ardell [17] in their TEM study of the precipitation kinetics in 7075 aluminium alloy reported the same structure and orientation relationship and nearly the same lattice parameters ($a = 0.496$ nm, $c = 1.403$ nm) for the η' precipitates. The above orientation relationship gives rise to twelve variants of η' precipitates in the aluminium matrix.

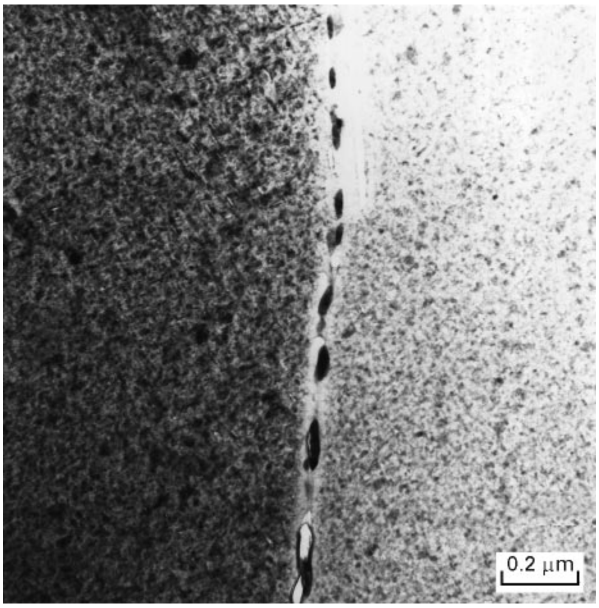

Figure 6 Bright-field transmission electron micrograph showing the equilibrium η precipitates decorating high-angle grain boundaries and narrow PFZs adjacent to the boundaries.

The lattice parameters of the aluminium matrix and the β′ (Al_3Zr) dispersoid particle were determined to be the same ($a = 0.4064$ nm) and the orientation relationship between them is given by

$$(001)\text{Al} \parallel (001)\text{Al}_3\text{Zr}$$

$$[100]\text{Al} \parallel [100]\text{Al}_3\text{Zr}$$

Accordingly, three variants of Al_3Zr precipitates are expected and their presence will give rise to superlattice reflections at the $\{001\}$ and $\{011\}$ positions in reciprocal space, as can be seen in the experimental and simulated SAD patterns in Fig. 5 (outlined by dashed line in Fig. 5d, e, f). A dark-field image taken using the (001) reflection in the $[100]\text{Al}\parallel[100]\text{Al}_3\text{Zr}$ SAD pattern in Fig. 5c, reveals the spheroidal Al_3Zr dispersoid particles to be of an average diameter of 24 nm and well dispersed in the aluminium alloy matrix (Fig. 4c).

In the experimental and simulated $[0\bar{1}1]\text{Al}\parallel[10\bar{1}0]\eta'$ SAD patterns in Fig. 5a and d, respectively, two variants of η′ (reflections outlined by the solid rectangles) with the $\langle 0001\rangle$ direction in each parallel to the two $\langle 111\rangle$ Al directions are present. Along the latter direction, η′ reflections occur at approximately every third position and the $\{0006\}$ reflections almost coincide with the corresponding $\{111\}$ reflections (i.e. $3d_{111}\,\text{Al} \sim d_{0002}\eta'$). Based on the measured lattice parameters and d-spacings, the misfit between these planes (or directions), $\delta = (3d_{111}\text{Al} - d_{0002}\eta')/(3d_{111}\text{Al})$, is calculated to be 0.009, which, in turn, implies that the interfaces between these planes are fully coherent during the early stages of formation. In the bright-field image recorded near this zone axis (i.e. $[0\bar{1}1]$Al), Fig. 4a, the η′ precipitates can be seen edge-on and their thinness gives rise to streaks along the corresponding $\langle 111\rangle\text{Al}\parallel\langle 0001\rangle\eta'$ directions in the SAD pattern (Fig. 5a). Apart from the above features, η′ reflections from a third variant, outlined by short solid lines in Fig. 5d, are also present in the experimental $[0\bar{1}1]$ pattern in Fig. 5a.

In the experimental and simulated $[111]\text{Al}\parallel[0001]\eta'$ SAD patterns in Fig. 5b and e, respectively, the $\langle 10\bar{1}0\rangle\eta'$ directions are parallel to the corresponding $\langle 0\bar{2}2\rangle$Al directions. Also, the $\{30\bar{3}0\}\eta'$ reflections almost coincide with the corresponding $\{0\bar{2}2\}$Al reflections. Based on the measured lattice parameters, the misfit between these directions (or planes), $\delta = (3d_{0\bar{2}2}\text{Al} - d_{10\bar{1}0}\eta')/(3d_{0\bar{2}2}\text{Al})$, is determined to be 0.02. Assuming that all this misfit is taken by the $b = 1/2[0\bar{1}1]$ dislocations in the aluminium matrix, the spacing between the dislocations is calculated to be approximately 14 nm, which implies that η′ precipitates smaller (in diameter) than this value will be completely coherent with the aluminium alloy matrix along this direction. The experimental $[111]$Al pattern (Fig. 5b) also shows additional weak reflections occurring from other η′ variants near the primary $\{11\bar{2}0\}\eta'$. However, these were not included in the simulated pattern in Fig. 5e. Finally, when dark-field images are recorded from the $(\bar{2}110)\eta'$ reflection contained in this pattern, the η′ precipitates appear hexagonal shaped (Fig. 4b), because they are being viewed parallel to the $\langle 0001\rangle\eta'$ direction, i.e. normal to the basal plane. Based on this observation and the one made near the $[0\bar{1}1]$Al beam direction (Fig. 4a), it is established that the η′ precipitates are hexagonal disc-shaped. The average thickness × diameter/edge-to-edge length of the η′ precipitates was measured to be 2 nm × 20 nm, which, based on the dislocation spacing calculation provided earlier, implies that these precipitates are, for the most part, fully coherent with the aluminium matrix. Closer inspection of the dark-field image in Fig. 4b reveals the presence of parallel, dark fringes within the η′ precipitates. These are probably the Moiré fringes, because a change in the spacing and orientation of the fringes could be observed upon changing the operating reflection (i.e. diffracting vector).

Finally, in the experimental and simulated $[100]$Al SAD patterns in Fig. 5c and f, respectively, reflections from two variants of η′ precipitates at every third $\{022\}$Al position, outlined by the solid lines in Fig. 5f, is seen. It should be noted, however, that reflections from four variants of the η′ should actually be present corresponding to two separate sets that have formed with their basal ($\{0001\}$) planes parallel to two different $\{111\}$Al planes and long axes ($\langle 10\bar{1}0\rangle$) parallel to each of the common $\langle 022\rangle$ directions on these planes. In effect, the reflections from the two variants of η′ that share the same $\langle 022\rangle$ direction (that are contained in the $[100]$ zone), coincide.

Disc-shaped precipitates of the equilibrium η phase (Mg_2Zn) having average dimensions of 15 nm × 55 nm were also observed decorating the grain boundaries, together with very narrow precipitate-free zones (PFZs) around the precipitates. This phase, which has a hexagonal structure with lattice dimensions $a = 0.521$ nm, $c = 0.860$ nm, is incoherent with the aluminium matrix [18]. Other independent studies have found the η phase to have nine different orientation relationships with the aluminium matrix [18–20].

TABLE II Tensile properties of aluminium alloy 7055-T7751 (mean values based on duplicate tests)

Orientation	Temperature (°C)	Elastic modulus[a] (GPa)	Yield strength		Tensile strength		Elongation (%)	Reduction in area (%)	ln (A_0/A_f) (%)
			(MPa)	(10^3 p.s.i.)	(MPa)	(10^3 p.s.i.)			
Longitudinal	27	70	610	90	630	92	12	16	16
	100	69	540	78	560	80	14	34	42
Transverse	27	70	620	91	650	94	10	16	16
	100	66	570	82	575	83	14	31	37

[a] Tangency measurement based on extensometer trace.

Lastly, other constituent phases are also present in this alloy, such as the Al_7Cu_2Fe phase (tetragonal structure with $a = 0.6336$ nm, $c = 1.487$ nm) [21–23], but these were not studied herein.

3.2. Tensile properties

A compilation of the uniaxial tensile properties of the alloy, for both the longitudinal and transverse orientations, at both ambient (27 °C) and elevated (100 °C) temperatures, is given in Table II. Duplicate samples were tested at each temperature and no significant variation between the pairs of samples was observed.

With an increase in test temperature from 27 °C to 100 °C, the 0.2% yield strengths and ultimate tensile strengths show a decrease for both the longitudinal (L) and transverse (T) orientations. The decrease in longitudinal yield strength is as high as 12%, whereas that of the transverse yield strength is only 8%. The corresponding decrease in both longitudinal and transverse tensile strengths is 12%. Ductility as expressed by elongation-to-failure, over a gauge length of 12.7 nm, increases at the elevated temperature (100 °C), for both the longitudinal and transverse orientations. The improvement is of the order of 17% for the longitudinal (L) orientation and as high as 40% for the transverse (T) orientation. The reduction-in-area (RA) of the alloy shows an improvement of over 100% for both orientations. The engineering stress–engineering strain curves of the alloy, for both the L and T orientations, at the two temperatures, are compared in Fig. 7. The monotonic strength coefficient, K, showed a nominal decrease with increase in test temperature, confirming the lower strength and strain hardening, n, capability of the aluminium alloy matrix with increase in test temperature (Fig. 8).

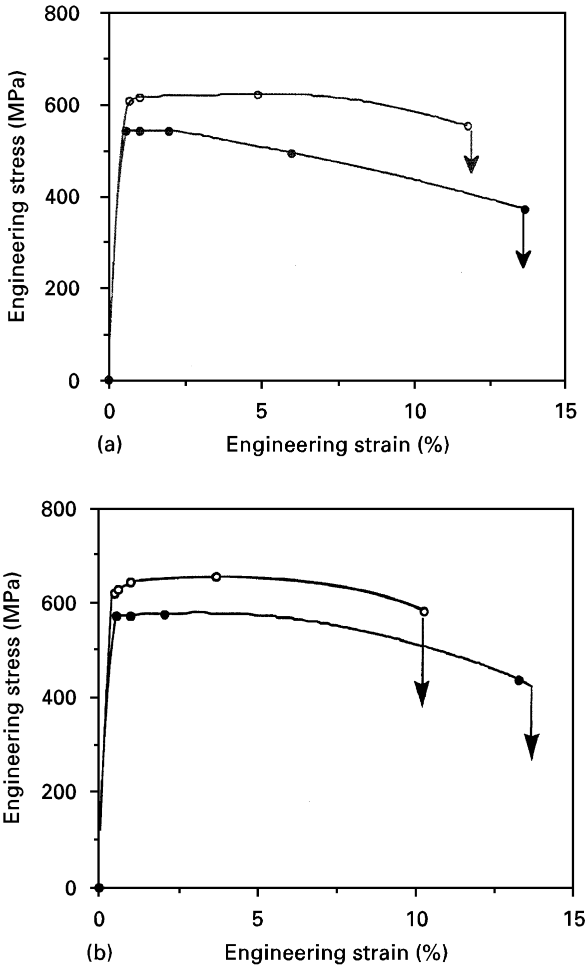

Figure 7 Comparison of the influence of temperature on engineering stress–engineering strain response of alloy 7055-T7751: (a) longitudinal specimen, (b) transverse specimen. (○) $T = 27$ °C, (●) $T = 100$ °C.

3.3. Tensile deformation and fracture

The tensile fracture surfaces are helpful in elucidating microstructural effects on strength, ductility and fracture properties of alloy 7055. Fractography of the tensile samples revealed the macroscopic fracture morphology to be identical for both the longitudinal and transverse specimens. However, for each orientation they were different at the two temperatures. The difference is believed to be associated with different proportions of the fracture mode and the individual features on the surface. Representative fracture features of the specimens for the longitudinal orientation are shown in Figs 9–11.

On a macroscopic scale, tensile fracture of the alloy deformed at ambient temperature (27 °C) was by shear, for both the longitudinal and transverse specimens, with the fracture surface oriented at approximately 40 °–45 ° to the major stress axis. The shear-type of fracture tends to minimize necking and any triaxial stress state and hydrostatic component that occurs in the necked region [24]. Fracture was bimodal comprising both transgranular and intergranular regions.

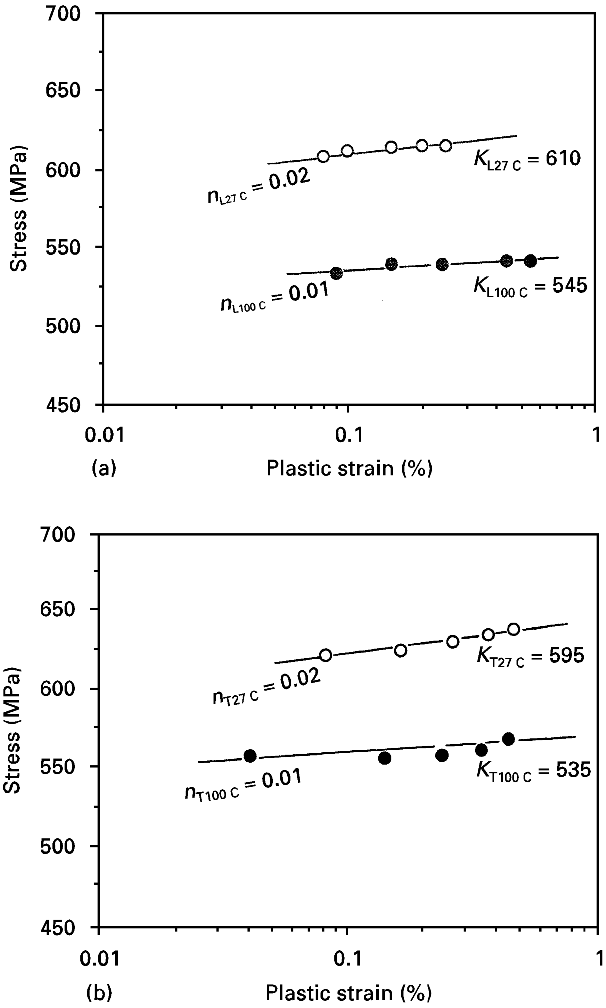

Figure 8 Monotonic stress–strain curves for aluminium alloy 7055-T7751: (a) longitudinal, (b) transverse. (○) $T = 27\,°\mathrm{C}$, (●) $T = 100\,°\mathrm{C}$.

Fracture of the deformed and failed tensile samples revealed:

(a) an overall macroscopically brittle appearance at low magnifications (Fig. 9a);

(b) at the microscopic level, features reminiscent of both ductile failure, namely voids and shallow dimples (Fig. 9c), and brittle failure, namely cracking along the grain and sub-grain boundaries (Fig. 9d).

The shallow dimples are the end result of the presence of smaller second-phase particles, that is, the zirconium dispersoids (β': Al_3Zr) and the equilibrium grain-boundary η precipitates. Because crack extension under quasi-static loading occurs at high stress intensities, comparable with the fracture toughness of the material, the presence of microscopic and macroscopic voids and intergranular cracking lowers the actual strain-to-failure associated with ductile fracture.

At the elevated temperature, the macroscopic fracture mode, for both the L and T specimens, was at 45 ° to the far-field stress (load) axis following a plane of maximum macroscopic shear stress. High-magnification observation revealed the transgranular regions to be covered with a population of voids of a range of sizes, and a bimodal distribution of dimples (Fig. 10a). The macroscopic voids were intermingled with fine microscopic voids. The applied far-field stress assists in the growth of these voids during the later stages of tensile deformation. Coalescence of the macroscopic voids is aided by the fine microscopic voids. During the coalescence stage, void–void interactions occur during which period void growth is accelerated. The macroscopic voids are created by fracture of the coarse intermetallic particles and constituent phases, and coalesce by impingement, that is, the voids growing until they touch each other. However, the more widely separated macroscopic voids coalesce by linking of the microscopic voids to form void sheets. The coalescence of fine microscopic voids initiated at the grain-boundary precipitates and particles results in a dimple-formation type intergranular fracture (Fig. 11). The transgranular fracture regions were covered with isolated pockets of shallow dimples. These dimples are associated with (i) the small insoluble phases, (ii) the equilibrium η precipitate, and (iii) the dispersoids.

During uniaxial straining, the tendency towards localized inhomogeneous deformation due to the shearing of the strengthening precipitates (η') dispersed in the alloy matrix results in a localization of strain. In fact, the occurrence of transcrystalline localization is favoured by the conjoint and mutually interactive influences of a high level of critical resolved shear stress and shearable precipitate particles. Repeated shearing of these particles leads to a progressive reduction of their size and a concomitant reduction in the overall resistance to the motion of dislocations. The number of dislocations (say N) that pass on a typical plane from the initiation of deformation until local slip ends, can be used as an indicator of slip localization [25]. The planar slip bands (Fig. 12), resulting from the interaction of the slip dislocations with the precipitate particles, impinge upon the grain and subgrain boundaries and cause a shear stress concentration at their point of impingement on the boundary. The magnitude of shear stress concentration associated with the pile-up of N dislocations is [26]

$$\tau^* = N\tau_e \qquad (1)$$

where τ_e is the resolved shear stress. When τ^* exceeds the crack nucleation stress at the grain-boundary regions, microcrack initiation and intergranular and/or inter-subgranular fracture are favoured. This is aided by:

(a) the presence of grain-boundary precipitates and particles;

(b) narrow precipitate-free zones (PFZs), which favour concentration of deformation and concomitant microcrack initiation at these regions.

Initiation of voids is favoured at the intersection of an inhomogeneous planar deformation band either with a grain-boundary particle or precipitate (Fig. 13). The applied far-field stress assists in the growth of these voids. The fine microscopic voids coalesce and the

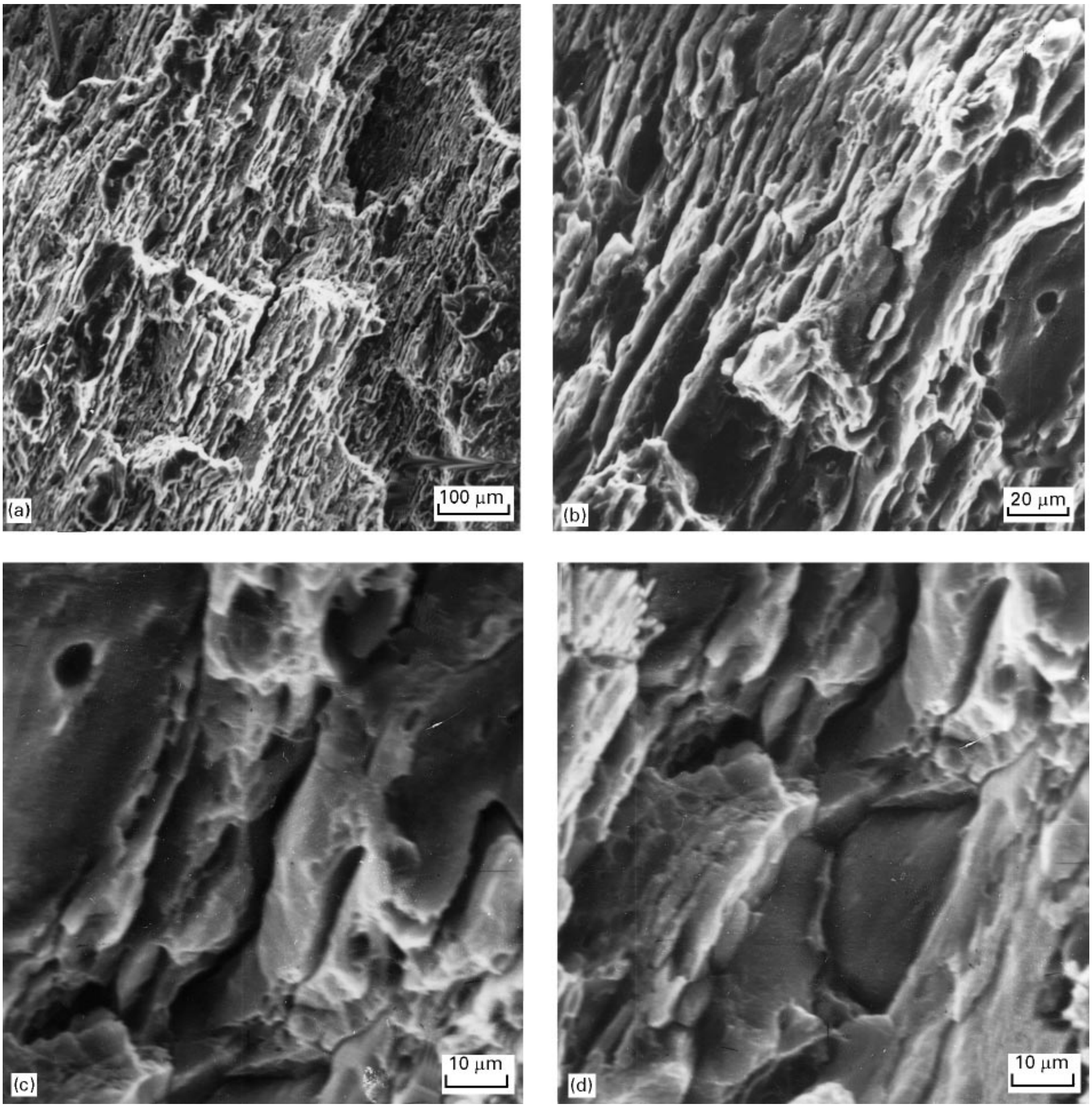

Figure 9 Scanning electron micrographs of the tensile fracture surface of the longitudinal specimen deformed at 27 °C showing (a) overall morphology, (b) high magnification of (a), (c) voids and shallow dimples, (d) cracking along the grain and subgrain boundaries.

TABLE III Monotonic parameters of aluminium alloy 7055–T7751

Orientation	Temperature (°C)	*n*	*K* (MPa)
Longitudinal	27	0.02	610
	100	0.01	545
Transverse	27	0.02	595
	100	0.01	535

halves of these voids are the shallow dimples found adjacent to the intergranular and inter-subgranular fracture regions. Void initiation at the coarse intermetallic and constituent phases is dictated by the conjoint influence of: (i) inclusion size, (ii) local stress and strain level, and (iii) matrix deformation characteristics. The iron-rich intermetallics (such as Al_7Cu_2Fe) and insoluble constituent particles coupled with a matrix microstructure which promotes localized inhomogeneous deformation, facilitates the nucleation and coalescence of voids at low to moderate stress levels. In fact, void nucleation at a coarse particle occurs when the elastic energy in the particle exceeds the surface energy of the newly formed void surfaces [27, 28]. Furthermore, assuming the coarse second-phase particles to be near-spherical in shape, the critical stress for particle cracking is

$$\sigma = (6\gamma E/q^2 d)^{1/2} \qquad (2)$$

where γ is the surface energy of the particle, q is the local stress concentration factor, E is the Young's modulus of the particle and d is the particle diameter. While satisfying this equation is a necessary condition, there must also exist a stress on the matrix–particle interfaces in excess of the interfacial strength [29].

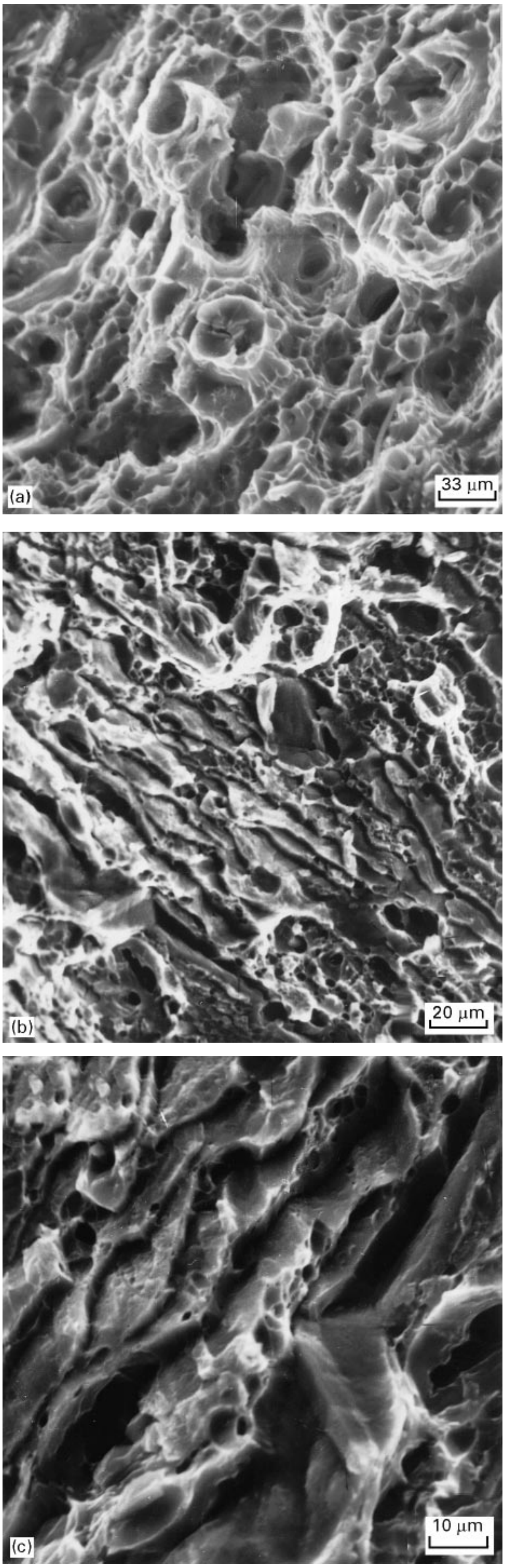

Figure 10 Scanning electron micrographs of the tensile fracture surface of the longitudinal specimen deformed at 100 °C, showing (a) overall morphology, (b) cracking along the high-angle grain boundaries, (c) high magnification of (b) showing distribution of voids and shallow dimples.

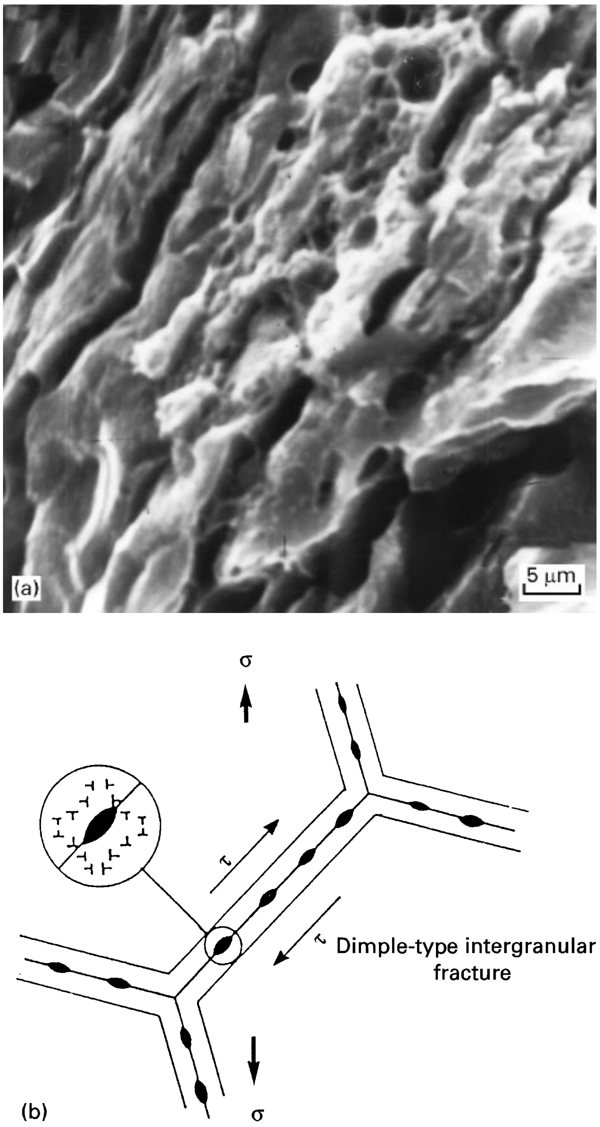

Figure 11(a) Scanning electron micrograph showing voids and dimples adjacent to the intergranular fracture regions. (b) Schematic diagram showing dimple-formation type intergranular fracture.

When the stress build-up at the particle–matrix interfaces reaches a critical value, void nucleation occurs by interface failure, that is, separation. For the alloy in the microstructural condition studied, the interface stress comprises the applied far-field stress, σ_A, and the normal stress due to blocked slip bands, σ_p [30]

$$\sigma_1 = \sigma_A + \sigma_P \tag{3}$$

When a critical value of σ_1 is reached, void nucleation occurs, provided sufficient elastic energy is available for the creation of new void surfaces. The macroscopic voids are created by fracture of the coarse intermetallic particles and constituent phases and they coalesce by impingement, that is, the voids growing until they touch each other. However, the more widely separated macroscopic voids coalesce by linking of the microscopic voids to form void sheets. The coalescence of fine microscopic voids initiated at the grain-boundary precipitates and particles results in a dimple-formation type intergranular fracture.

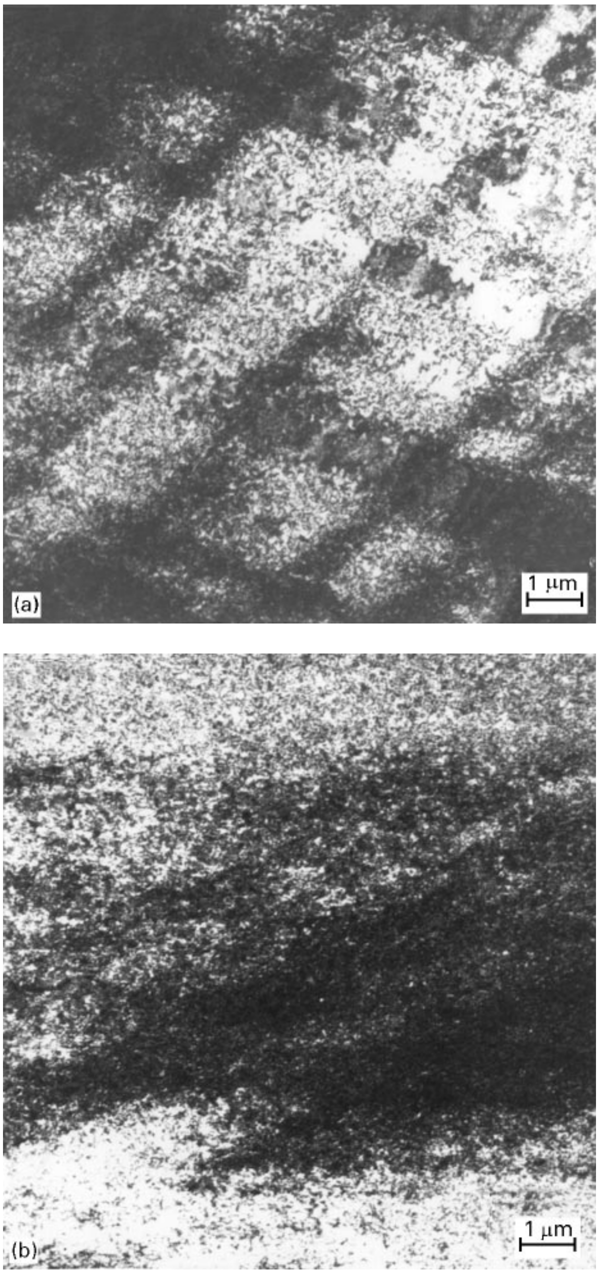

Figure 12 Bright-field transmission electron micrographs showing planar deformation bands in aluminium alloy 7055-T7751 at (a) 27 °C, (b) 100 °C.

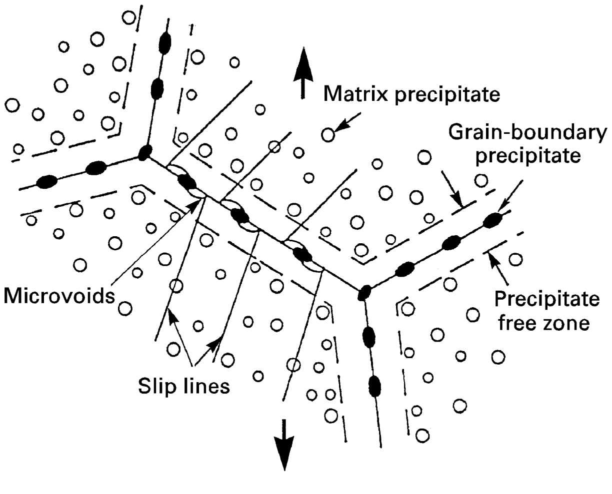

Figure 13 Schematic diagram showing the deformation process in the presence of a narrow precipitate-free zone and grain-boundary precipitates.

4. Conclusions

1. The alloy has a partially recrystallized microstructure with the large recrystallized grains flattened and elongated in the longitudinal direction. The insoluble intermetallic particles and partially soluble constituent phases were observed to be isolated and randomly distributed along the three orthogonal directions of the rolled plate.

2. The principal strengthening phase in this Al–Zn–Mg–Cu alloy is the η' precipitate. This precipitate phase was determined to be hexagonal disc-shaped with average dimensions of 2 nm × 20 nm, fully coherent with the aluminium matrix, and to have a hexagonal structure with $a = 0.5078$ nm and $c = 1.395$ nm, and an orientation relationship with the aluminium matrix given by $(1\,1\,1)\mathrm{Al}\,||\,(0\,0\,0\,1)\eta'$; and $[0\,\bar{1}\,1]\mathrm{Al}\,||\,[1\,0\,\bar{1}\,0]\eta'$.

3. A small volume fraction of randomly dispersed spheroidal Al_3Zr precipitates of average size 200 nm were also observed. The high-angle grain boundaries were decorated by the equilibrium η precipitates. Narrow precipitate-free zones were present around the high-angle grain boundaries but not at the sub-grain or low-angle grain boundaries.

4. In the T7751 condition the yield strength and ultimate tensile strength of the alloy accord reasonably well for the longitudinal and transverse orientations. The strength of the alloy marginally decreased with increase in test temperature.

5. The elongation-to-failure showed a marginal improvement with increase in temperature. However, the reduction in area showed over 100% improvement with increase in temperature.

6. Fracture morphology, at a given temperature, was identical for both the longitudinal and transverse specimens. Macroscopic fracture of the alloy was by shear, while microscopic fracture revealed features reminiscent of both brittle and locally ductile mechanisms, that is, combination of cracking along the grain and subgrain boundaries coupled with ductile microvoid formation, growth and coalescence.

7. Tensile deformation structures revealed the predominant mode to be inhomogeneous with the occurrence of planar slip bands. The slip bands were less intense at the elevated temperature.

Acknowledgements

This research was supported in part by The University of Akron (through a Faculty Research Grant no 2-07299 to Dr Srivatsan) and The University of Cincinnati. The authors extend their sincere thanks and appreciation to the Aluminum Company of America (ALCOA Technical Center: *Program Manager* Dr Gary H. Bray) for providing the material used in this study.

References

1. J. G. KAUFMAN, "Design of Aluminium Alloys for High Toughness and High Fatigue Strength", 40th Meeting of Structures and Materials Panel, NATO, Brussels, Belgium, April 1975.

2. R. E. SANDERS Jr and E. A. STARKE Jr, *Metall. Trans.* **6A** (1978) 1087.
3. M. V. HYATT and W. E. QUIST, AFML Technical Report, TR-67-329 (Air Force Materials Laboratory, Dayton, OH, 1967).
4. J. T. STALEY, Technical Report, Naval Air Systems Command, Contract M00019-71-C-0131, May 1972.
5. *Idem*, in "ASTM Symposium on Properties as Related to Toughness", Montreal, Canada, June 1975.
6. J. S. SANTNER, AFML Technical Report, TR-76-200 (Air Force Materials Laboratory, Dayton, OH, 1977).
7. F. OSTERMANN, *Metall. Trans.* **2** (1971) 2897.
8. E. DiRUSSO, M. CONSERVA, F. GATTO and H. MARKUS, *ibid.* **4** (1973) 1133.
9. W. H. REIMANN and A. W. BRISBANE, *Eng. Fract. Mech.* **5** (1973) 67.
10. D. S. THOMPSON, S. A. LEVY and D. K. BENSON, in "Third International Conference on Strength of Metals and Alloys", Cambridge, UK (1973) pp. 119–23.
11. J. E. VRUGGINK, Technical Report, FA-TR 76073, April 1977.
12. H. SULINSKI and J. WALDMAN, " Frankford Arsenal Summary Report", Philadelphia, PA, July 1976.
13. J. T. STALEY and R. L. ROLF, in "International Symposium on Light Metals" (The Minerals, Metals and Materials Society, 1993).
14. J. T. STALEY in "Encyclopedia of Physical Science", Vol. 1 (1992) pp. 591–8.
15. ASTM Standard E-8-93, Tension Testing of Metallic Materials (American Society for Testing and Materials, Philadelphia, PA, 1993).
16. T. S. SRIVATSAN, K. YAMAGUCHI and E. A. STRAKE Jr, *Mater. Sci. Eng.* **83** (1986) 87.
17. J. K. PARK and A. J. ARDELL, *Metall. Trans.* **14A** (1983) 1957.
18. P. A. THACKERY, *J. Inst. Metals.* **96** (1968) 228.
19. J. D. EMBURY and R. B. NICHOLSON, *Acta Metall.* **13** (1965) 403.
20. H. P. DEGISCHER, W. LACOM, A. ZAHRA and C. ZAHRA, *Z. Metallkde* **71** (1980) 231.
21. M. G. BROWN and D. J. BROWN, *Acta Crystallogr.* **9** (1956) 911.
22. R. AYER, J. Y. KOO, J. W. STEEDS and B. K. PARK, *Metall. Trans.* **16A** (1985) 1925.
23. S. WANG, LI CHUNZHI, B. WEIMIN and Y. MING GAO, *Acta Metall. Sinica* **25** (1989) 10.
24. W. X. FENG, F. S. LIN and E. A. STARKE Jr, *Metall. Trans.* **15A** (1984) 1209.
25. J. M. DUVA, M. A. DAUBLER, E. A. STARKE Jr, and G. LUTJERING, *Acta Metall.* **36** (1988) 585.
26. J. P. HIRTH and J. LOTHE, "Theory of Dislocations" (McGraw Hill, New York, 1968) pp. 694–700.
27. R. H. VAN STONE and J. A. PSIODA, *Metall. Trans.* **6A** (1975) 672.
28. R. H. VAN STONE, T. B. COX, J. R. LOW Jr and J. A. PSIODA, *Int. Metal. Rev.* **30** (1985) 157.
29. A. S. ARGON, J. IM and R. SAFOGLU, *Metall. Trans.* **6A** (1975) 825.
30. T. S. SRIVATSAN, D. LANNING and K. K. SONI, *J. Mater. Sci.* **28** (1993) 3205.

Received 2 July
and accepted 23 October 1996